

Prediction, experimental results and analysis of the ITER TF insert coil quench propagation tests, using the 4C code

R Zanino¹ , R Bonifetto¹, A Brightenti¹, T Isono², H Ozeki² and L Savoldi¹

¹ NEMO Group, Dipartimento Energia, Politecnico di Torino, Torino, Italy

² National Institutes for Quantum and Radiological Science and Technology, Naka, Japan

E-mail: roberto.zanino@polito.it

Received 6 August 2017, revised 22 November 2017

Accepted for publication 30 November 2017

Published 29 January 2018



Abstract

The ITER toroidal field insert (TFI) coil is a single-layer Nb₃Sn solenoid tested in 2016–2017 at the National Institutes for Quantum and Radiological Science and Technology (former JAEA) in Naka, Japan. The TFI, the last in a series of ITER insert coils, was tested in operating conditions relevant for the actual ITER TF coils, inserting it in the borehole of the central solenoid model coil, which provided the background magnetic field. In this paper, we consider the five quench propagation tests that were performed using one or two inductive heaters (IHs) as drivers; out of these, three used just one IH but with increasing delay times, up to 7.5 s, between the quench detection and the TFI current dump. The results of the 4C code *prediction* of the quench propagation up to the current dump are presented first, based on simulations performed *before* the tests. We then describe the experimental results, showing good reproducibility. Finally, we compare the 4C code predictions with the measurements, confirming the 4C code capability to accurately predict the quench propagation, and the evolution of total and local voltages, as well as of the hot spot temperature. To the best of our knowledge, such a predictive validation exercise is performed here for the first time for the quench of a Nb₃Sn coil. Discrepancies between prediction and measurement are found in the evolution of the jacket temperatures, in the He pressurization and quench acceleration in the late phase of the transient before the dump, as well as in the early evolution of the inlet and outlet He mass flow rate. Based on the lessons learned in the predictive exercise, the model is then refined to try and improve *a posteriori* (i.e. in interpretive, as opposed to predictive mode) the agreement between simulation and experiment.

Keywords: superconducting coil, quench, ITER, prediction, thermal-hydraulic simulation

(Some figures may appear in colour only in the online journal)

1. Introduction

The safe application of any code to predictive (or design) exercises concerning forthcoming or future superconducting (SC) fusion machines, like ITER, JT-60SA, or DEMO, should in principle be preceded by, and rely on, its successful verification and validation, i.e. on a good agreement between simulations and measurements, aimed at confirming that the code implements the right model and that the model equations are correctly solved. Furthermore, separate validation exercises should be conducted for different transients (e.g., stability, AC

losses, quench, cooldown, etc), in view of the different physics and time scales involved. Also, it should be important to distinguish between validation exercises where the simulations are performed after/with/taking advantage of the knowledge of the results of the measurements, and rigorously predictive (i.e. blind) validation, where the simulations are performed *before*/without the knowledge of the results of the measurements, which is obviously much harder. Indeed, code validation, with special reference to predictive validation, is considered a very important and needed step in different big communities, e.g., the American Institute of Aeronautics and Astronautics, the American Nuclear

Society or the American Society of Mechanical Engineers, where the question of the verification and validation of computational modeling has been developed in the last few decades to a level of unprecedented maturity and rigor, see for instance [1, 2].

Quench propagation in cable-in-conduit conductors (CICCs) or magnets for nuclear fusion has attracted the interest of the superconductor science and technology community for many years. After the first studies in the 1980s [3], the quench experiment on long length was carried out in the mid 1990s on an ITER-like (albeit sub-size) CICC, characterized by the presence of a central cooling channel [4–6]. In the first decade of this century, the major role in increasing the database related to this fundamental phenomenon was played by the tests of the ITER insert coils [7–11], which gave rise to a series of computational studies specifically devoted to the topic [12–17].

However, notwithstanding the non-negligible extent of the quench-related database today, the validation of the existing thermal-hydraulic (TH) models and computational tools for this fundamental transient in SC magnets is still far from being a routine step, and if we talk about predictive validation, no such exercise can be found in the literature, to the best of our knowledge.

With the above-mentioned background in mind, and following the roadmap proposed in [18] to confirm the reliability of the existing TH codes for SC magnets, we have taken advantage of the (then) forthcoming second ITER toroidal field (TF) insert (TFI) [19] coil test, to try and confirm the predictive capabilities of the state-of-the-art 4C code [20]: a set of simulations of quench propagation in the TFI was performed, as adherent as possible in input to the TFI test program but still *before* the test. As a proof of the blind nature of these simulations, selected results thereof were distributed among the members of the testing group before the tests were actually performed.

The paper is organized as follows: we first introduce the relevant experimental setup and available diagnostics in the TFI, which were of course the fundamental input of the simulations; then we present the predictive 4C quench model and a selection of its results; then we describe the experimental results of all the quench tests performed in the TFI; then we compare the predictions with the measurements; finally, we introduce an upgrade of the 4C model, developed on the basis of the lessons learned in the predictive exercise, and show how this improves the interpretive capabilities of the 4C code as far as the TFI quench propagation is concerned.

2. Experimental setup

The TFI coil, see figure 1, is a 43 m long single-layer solenoid wound in the grooves of a stainless-steel (SS) mandrel, using one of the Nb₃Sn circular CICC (see figure 2) adopted for the actual ITER TF coils and cooled with supercritical He in forced circulation at 4.5 K. The TFI is so far the last item in the above-mentioned series of ITER Insert Coils [7–11], all tested in the bore of the ITER Central Solenoid Model Coil (CSMC) [21] at Naka, Japan, in conditions relevant for the

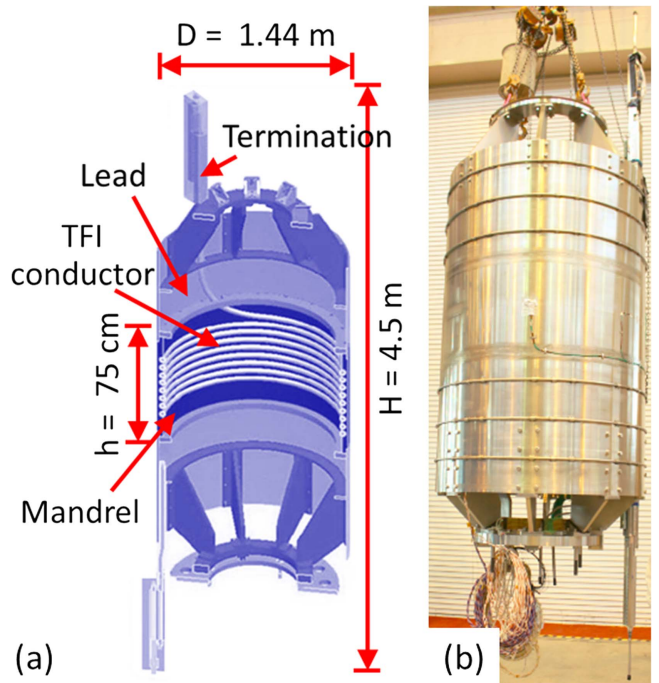


Figure 1. (a) Section of the TFI assembly and (b) picture of the TFI before installation in the bore of the CSMC (courtesy of QST).

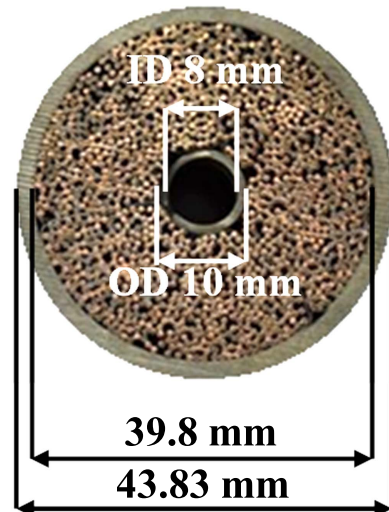


Figure 2. Cross section of the TFI conductor.

actual ITER operation. Tables 1 and 2 report the main geometrical and scaling parameters [24] for the TFI conductor.

Several tests were devoted to the study of quench propagation, aimed at the assessment of the hot spot in the conductor. The quench was initiated pulsing an inductive heater (IH), wrapped around the conductor at mid length of the TFI, at increasing energies. Different delay times (3, 5, 7.5 s) after quench detection (QD) were imposed, before the 68 kA TFI current was dumped on an external resistor.

The TFI coil is well equipped with a set of diagnostics that includes thermometers, pressure taps and flow meters at the insert inlet and outlet, as well as several voltage taps and Cernox thermometers along its length, see figure 3.

Table 1. Main geometrical parameters for the TFI conductor [22, 23].

Jacket external diameter (mm)	43.83
Jacket internal diameter (mm)	39.8
Void fraction in the bundle region (%)	31.3
Central channel ID/OD (mm)	8/10
Total He cross section (mm ²)	420
Number of strands (SC + Cu)	900 + 522
Strand diameter (SC/Cu) (mm)	0.822/0.821
Cos(θ)	0.9699
Wrapping area (mm ²)	34
Cabling pattern	((2 SC + 1 Cu) × 3 × 5 × 5 + (3 Cu × 4 Cu)) × 6

Table 2. ITER style $I_C (B, T, \varepsilon)$ parameterization for the TFI conductor [23].

$C [A \times T]$	33×10^3
$B_{c20m} [\text{T}]$	32.35
$T_{c0m} [\text{K}]$	16.22
$p [-]$	0.84
$q [-]$	2.57
$C_{a1} [-]$	47.02
$C_{a2} [-]$	11.76
$\varepsilon_{0a} [-]$	2.31×10^{-3}
$\varepsilon_m [-]$	3.97×10^{-3}

The TFI quench tests were planned (and eventually performed) in the expected operating conditions for the ITER TF, i.e. transport current $I_{\text{TFI}} = 68 \text{ kA}$ and peak magnetic field $B_{\text{peak}} = 11.8 \text{ T}$. As in all previous ITER Insert Coil tests, the quench was planned to be initiated pulsing for 40 ms the inductive heater IH02, approximately located at the central turn of the conductor. (Eventually, also a single test simultaneously pulsing two IHs was performed.) This explains the non-uniform distribution of the diagnostics along the coil length, i.e. their refinement close to the IH region.

The definition of QD is based on the value of the total voltage (ITF-VD-ALL) measured across the TFI. While the coil is in operation, at any time t the ITF-VD-ALL signal is integrated along the conductor over the previous 0.1 s by the QD system: if the result is larger than the prescribed threshold of 0.01 V × s, a quench is detected, see figure 4. In that case, the quench freely propagates for a prescribed delay time (t_{delay}), after which a signal triggers the dump of the TFI current onto a dump resistor, by opening the coil electric circuit. (About 0.45 s after the TFI dump, also the CSMC current is dumped to avoid additional heat deposition in the TFI because of combined AC losses, but we will not consider this phase in the paper, as all of our simulations will stop at the dump of the TFI.)

A set of delay times was planned in the test program, increasing up to a maximum $t_{\text{delay}}^{\max} = 7.5 \text{ s}$. This delay time was chosen in order to assess the TF conductor behavior after a quench, featuring a Joule energy deposition as similar as possible to that of a detected quench of a TF coil in ITER. According to the ITER design criteria [25], the QD and switch opening will take $\tau_{\text{det}} = 2 \text{ s}$, during which the coil will

still operate at full current I_0 . In this phase, the energy deposition $E_{\text{J,det}}$ is

$$E_{\text{J,det}} = RI_0^2 \tau_{\text{det}} \quad (1)$$

then the current will undergo a fast discharge

$$I(t) = I_0 \exp(-t/\tau_{\text{dump}}) \quad (2)$$

with a time constant $\tau_{\text{dump}} = 11 \text{ s}$. The energy $E_{\text{J,dump}}$ deposited during this exponential decay, until the coil has been fully discharged, and under the assumption that the resistance is constant, is

$$E_{\text{J,dump}} = R \int_{t_{\text{dump}}}^{+\infty} (I(t))^2 dt = RI_0^2 \frac{\tau_{\text{dump}}}{2} \quad (3)$$

so that the total energy deposited in an ITER TF coil during a quench is

$$E_{\text{J}} = E_{\text{J,det}} + E_{\text{J,dump}} = RI_0^2 \left(\tau_{\text{det}} + \frac{\tau_{\text{dump}}}{2} \right). \quad (4)$$

As in the TFI

$$E_{\text{J}} = RI_0^2 \left(t_{\text{delay}} + \frac{\tau_{\text{dump, TFI}}}{2} \right) \quad (5)$$

and $\tau_{\text{dump, TFI}}$ is negligibly small ($\sim 0.1 \text{ s}$) with respect to t_{delay} , $t_{\text{delay}}^{\max} = \tau_{\text{det}} + \tau_{\text{dump}}/2$.

3. Quench predictions

The 4C code has been used for all the simulations presented in this paper.

The previous validation and application history of the 4C code covers a large set of experiments, including the two ITER model coils [26, 27], for which, however, no quench tests were ever performed, and the above-mentioned insert coils. Very different types of transients were considered, including the quench, but always in an interpretive form (i.e., after the tests were performed).

In fact, for the 4C code we can claim so far only one strictly predictive (i.e. blind) validation test, namely the study of different types of pulsed heat load smoothing scenarios based on the use of the HELIOS SHe loop [28]. To the best of our knowledge, that was the only strictly predictive (i.e. blind) validation test of any TH code for SC fusion magnets before the present paper.

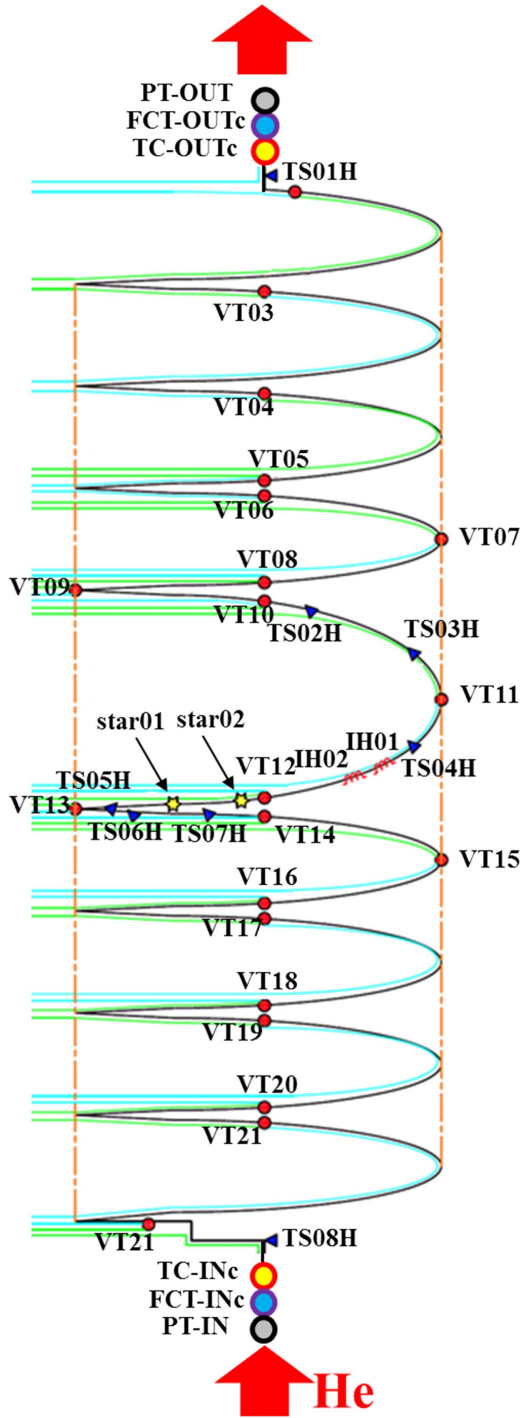


Figure 3. Sketch of the available diagnostics installed along the coil length [23]: VT_{xx} and star_{xx} voltage taps, TS_{xx} (Cernox, on the jacket) and TC-_{xx} (Carbon, on the He pipes) thermometers, PT-_{xx} pressure taps and FCT-_{xx} flow meters. IH02 indicates the inductive heater used for triggering most of the quench tests. The thick red arrows show the direction of the He flow.

3.1. Simulation setup

For the TFI quench prediction we focused on the case $t_{\text{delay}} = t_{\text{delay}}^{\max}$ which obviously includes the quenches at shorter t_{delay} as the quench is computationally reproducible by definition (i.e., the first, e.g., 3 s of the propagation of a 7.5 s

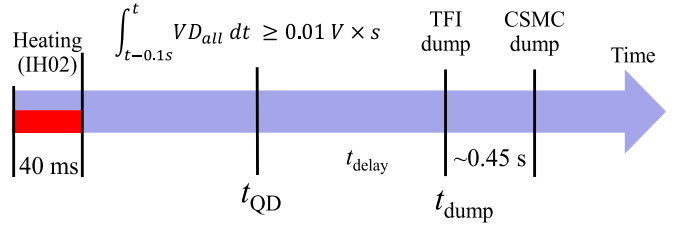


Figure 4. Graphical representation of the quench timeline, with TFI and CSMC current dumps.

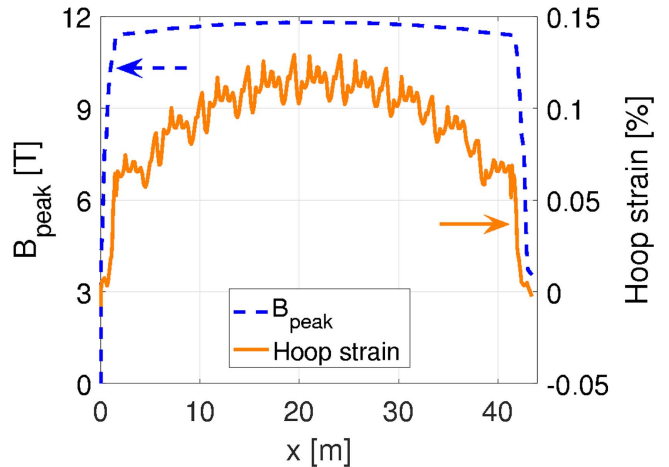


Figure 5. Peak magnetic field (dashed blue, left y-axis) and hoop strain (solid orange, right y-axis) distributions along the TFI.

delay quench will automatically coincide with the whole propagation of a 3 s delay quench in the simulation).

The parameters which must be set in input include:

- The identification of the computational domain and the respective boundary conditions, if needed → we simulate the entire conductor, including the joint region, and we impose fixed pressure at the TFI inlet and outlet, $p_{\text{in}} \sim 5.6$ bar, $p_{\text{out}} \sim 5.5$ bar for the sake of simplicity. We impose also a fixed inlet temperature $T_{\text{in}} = 5.7$ K, as long as no backflow occurs at the coil inlet;
- The magnetic field map $B(x)$ and hoop strain distribution along the conductor → we use the maps shown in figure 5 [29]; note that the total strain is obtained summing up the contribution of the hoop strain, the thermal strain (-0.7%) and the extra strain (-0.04%), calibrated by means of the analysis of current sharing temperature (T_{CS}) measurements in the TFI, as recently done for the central solenoid insert coil (CSIC) [30];
- The value of the conductor n -index = 5 for the SC-to-normal state transition region, calibrated by means of the analysis of the TFI T_{CS} measurements;
- The initial condition: imposed linear pressure drop between p_{in} and p_{out} (resulting in an initial mass flow rate of $\sim 8 \text{ g s}^{-1}$) and temperature profile obtained running a simulation with prescribed T_{in} until a steady-state is reached without power input from the IH;
- The linear power density $q'(x, t)$ to be applied to the conductor and its repartition between cable and jacket, to

properly mimic the power deposition by the IH → this is in principle a delicate choice, but experience from the simulation of many quenches in other ITER insert coils teaches that, as opposed to the quench initiation, quench *propagation* is not significantly affected by these parameters. Therefore, we chose a sufficiently high energy to get a quench propagation in the system (~ 110 J) and deposited it uniformly both in time (40 ms duration) and in space along the conductor (112 mm, coinciding with the IH length). 80% of the power was deposited in the jacket and the rest in the cable;

- The constitutive relations for the 1D conductor model, and namely the friction factors for the cable bundle and for the central channel region, the heat transfer coefficients (HTCs) between the different conductor constituents and the HTC between conductor and mandrel, which were found best-fitting with the 4C code another set of pure TH (i.e., without current) independent TFI data [31];
- From the numerical point of view, adaptive time-step (from 0.5 to 100 ms) and mesh size (from 0.25 to 100 mm) have been adopted as a result of a dedicated convergence study.

3.2. Simulation results

We present in this section a selection of the results of the predictive simulations, aimed at giving to the reader an idea of the wealth and level of detail of the information which can be extracted from a code run. Moreover, they focus on the evolution of some of the quantities for which a direct comparison with the measurements will be presented below. These quantities are: the local voltages V_{loc} across pairs of neighboring voltage taps close to the IH; the maximum strand temperature; the maximum pressurization in the conductor, localized under the IH02, with respect to the instant ($t = 0$) when the IH is switched on; the inlet and outlet He mass flow rates dm/dt . All of the evolutions are reported in these figures as functions of

$$t^* \equiv t - t_{QD}, \quad (6)$$

whereas the initial time in the plots corresponds to $t = 0$ s.

Figure 6 clearly shows the downstream and upstream propagation of the quench (progressive take-off of the voltage signals downstream and upstream of the IH, respectively).

The knees on the local voltage traces, for instance at $t^* \sim 0$ s on ITF-VD-1112g, or at $t^* \sim 2$ s on ITF-VD-1011g and ITF-VD-1213g, are due to the fact that, at those times, the whole length between the respective taps has become normal. The further voltage increase becomes then slower, as it is only due to the temperature increase and related increase of the Cu resistivity.

While from these data the evolution of the total computed voltage across the coil can be easily deduced (shown below in the comparison with the experiment), they are used here to deduce the propagation of the quench front, represented in the (x, t) characteristics plane in figure 7. The passage of the quench front beyond a voltage tap is assumed to occur when the voltage measured between that voltage tap and its

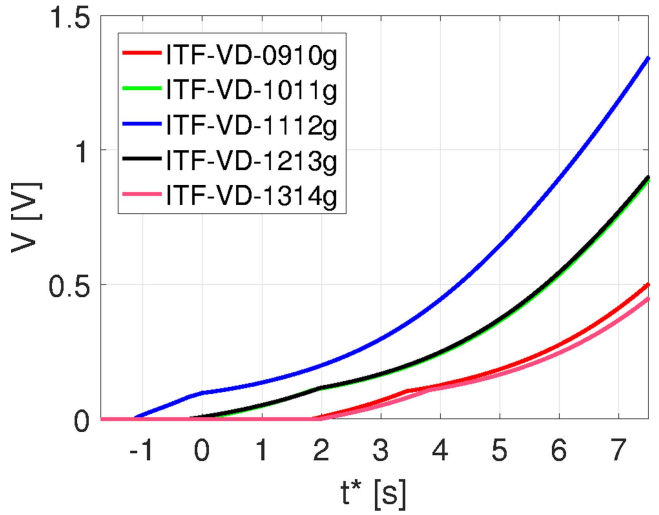


Figure 6. Predicted evolution of the local voltages.

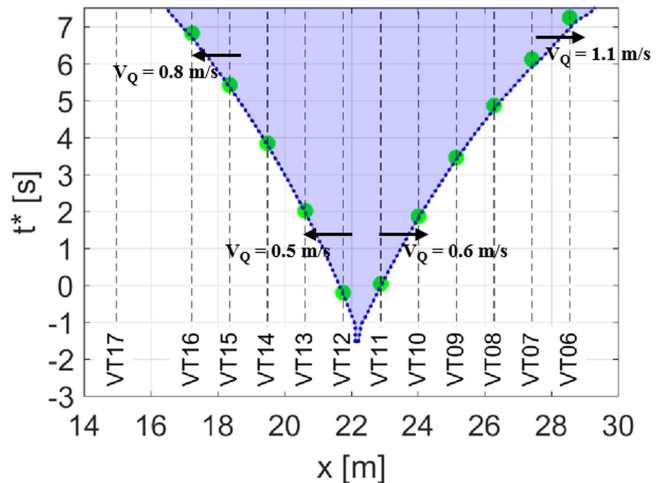


Figure 7. Predicted normal zone propagation with 7.5 s delay in the characteristic (x, t) plane. Symbols: passage of the quench front beyond a voltage tap, assumed to occur when the local voltage overcomes 1 mV; dotted lines: trajectory of the points where $I = I_C$.

neighbor ahead of the quench front reaches the conventional threshold of 1 mV. This is done in order to perform a fair comparison with the experimental data, for which the same voltage threshold is adopted to detect the entrance of the quench front in the space between two voltage taps, see below. In addition, the set $x_Q(t)$ of the points where $I = I_C$ is also reported, as it better identifies the quench front propagation in the simulation. The approximate quench propagation speed V_q between two neighboring voltage taps can then be easily deduced from the time needed to propagate from one voltage tap to the neighboring one, and is also reported in figure 7, showing what appears to be a rather ubiquitous feature of the quench in ITER CICCs, namely its progressive acceleration [32].

Just as in the case of the recent quench test of the CSIC [17], the model can be used to confirm that also in the TFI the quench is a classical pressure-driven quench, propagating with the area weighted average of the He flow speed in the

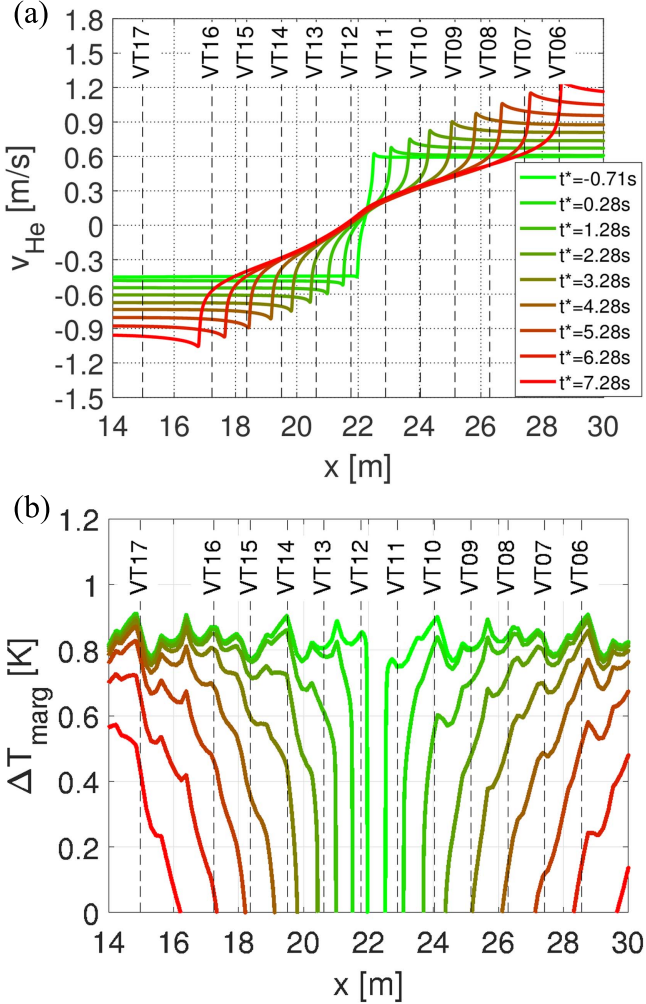


Figure 8. (a) Predicted area-weighted average He speed distribution in the TFI central zone during quench propagation at different times t^* . (b) Predicted distribution of the temperature margin in the TFI central turns during quench propagation at different times t^* .

two CICC regions at the quench front, see figure 8(a). The preheating of the cable ahead of the quench front originates a broader and broader region with relatively low margin ahead of the quench front as time goes by, as reported in figure 8(b), which favors the quench acceleration.

The local voltage signal across the IH (ITF-VD-1112g in our case), shown in figure 6, is also routinely used, together with the temperature dependence of the Cu resistivity, to experimentally estimate the hot spot temperature ($T_{\text{hot spot}}$)—the so-called virtual thermometer, see figure 9. Assuming that the cable temperature is uniform between the voltage taps VT_{11} and VT_{12} embracing IH02, i.e. T_{1112} , the temperature of the cable in the normal zone can be extracted from the measured $VD_{1112} = VT_{12} - VT_{11}$, following a well-known procedure [12, 15]. Solving for $T_{1112} = T_{\text{hot spot}}$ the implicit equation (7):

$$VD_{1112} = \rho_{\text{Cu}}(T_{1112}) \times (L_{1112}/A_{\text{Cu}}) \times I_{\text{TFI}}, \quad (7)$$

where ρ_{Cu} is the copper electrical resistivity, L_{1112} is the strand length between VT_{11} and VT_{12} , A_{Cu} is the total copper

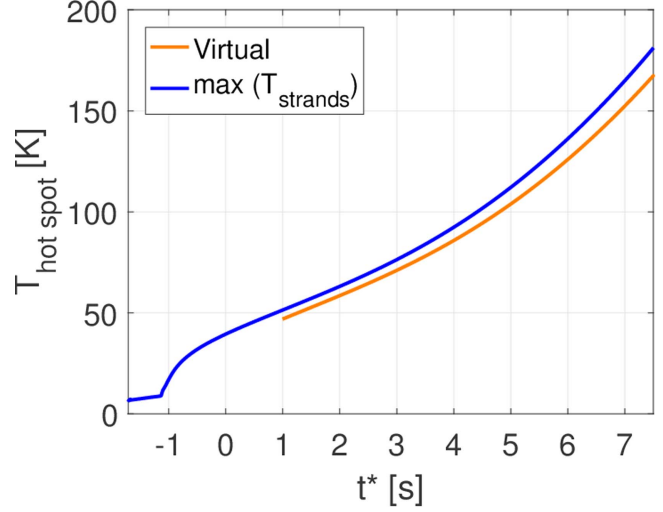


Figure 9. Predicted virtual hot spot temperature (solid orange) and maximum strand temperature (solid blue) evolutions.

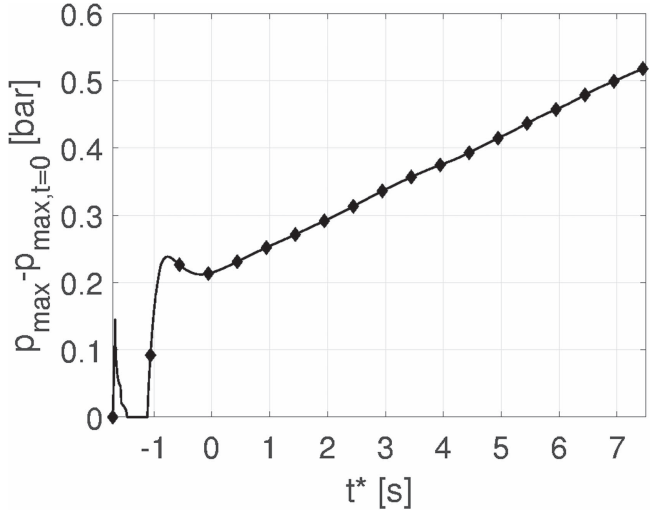


Figure 10. Maximum pressurization, with respect to the initial value, occurring in the conductor under IH02 during the quench propagation.

cross section and assuming, for sake of simplicity and conservative reasons, that all the current flows in the Cu.

The maximum strand temperature, also shown in figure 9, is obviously always above the virtual thermometer signal, since the strand temperature profile across ITF-VD-1112g will not be uniform but peaked. On the other hand, the difference between the two is not that big in this case, thanks also to the small distance (1.132 m) between VT_{11} and VT_{12} .

The coil starts pressurizing during the inductive pulse, see figure 10, and on the sound timescale also the mass flow rate at the coil boundaries reacts, leading to backflow at the inlet, see figure 11.

Then the pressure decays rather quickly to the initial value, until the Joule heating due to the formation of the normal zone takes off. At that time the pressure rises again very quickly, until again on the sound timescale a strong expulsion of helium, both at the coil inlet and outlet, see figure 11, leads to a second slower pressurization phase.

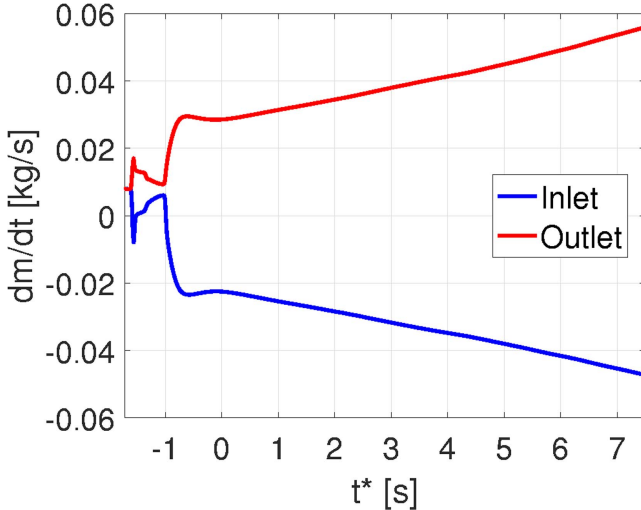


Figure 11. Predicted mass flow rate evolution at the coil boundaries during quench propagation.

4. Experimental results

Table 3 reports a summary of the IH-driven quench tests performed on the TFI, with distinguishing features in boldface.

The test results have a nice reproducibility for what concerns both the global (V_{tot}) and the local voltages, see figure 12. (Note that the QD time used in the definition of t^* is now the experimental one, i.e. t^* here and in the previous section are not exactly coincident.)

The normal zone obviously initiates between VT_{11} and VT_{12} , as the IH is located there.

The flattening of the experimental trace of the local voltage ITF-VD-1112g for $t^* > \sim 6.5$ s after the QD is due to the saturation of the sensor.

The quench front propagation, deduced as explained above from the local voltage signals take-off, is reported in figure 13 for all the IH-driven quench tests, showing again excellent reproducibility. The normal zone propagation is almost symmetric with respect to the IH location and just a little faster in the downstream direction, because of the background (initial) He flow. The quench fronts progressively accelerate both upstream and downstream, from an initial speed of $\sim 0.5 \text{ m s}^{-1}$ to more than 1.5 m s^{-1} , as estimated from the time needed to propagate from one voltage tap to the neighboring one in figure 13.

The hot spot temperature, deduced from the local voltage signals as explained above, also suffers of the above-mentioned saturation, see figure 14. An experimental assessment of the maximum temperature reached by the conductor at the time of the dump in the quench test characterized by the longest delay time is then unfortunately possible only through extrapolation.

The measured jacket temperature evolution at different locations, see figure 15, is not as perfectly reproducible in the different quench tests as the previously considered variables, but shows a spread up to 3.5 K. Furthermore, TS03 shows a somewhat odd behavior, with a trace that does not run parallel to the others, but instead grows much more slowly, possibly

Table 3. Summary of the IH-driven quench tests performed on the TFI.

Delay (s)	Shot #	IH	V_{DC} (V)	$\int I^2 dt$ ($\text{A}^2 \text{s}$)
3	109 – 11	IH02	80.0	640
5	110 – 6	IH02	80.0	652
7.5	113 – 10	IH02	82.7	676
3	118 – 8	IH02 + IH01	132.2	711
3	120 – 5	IH02	90.5	806

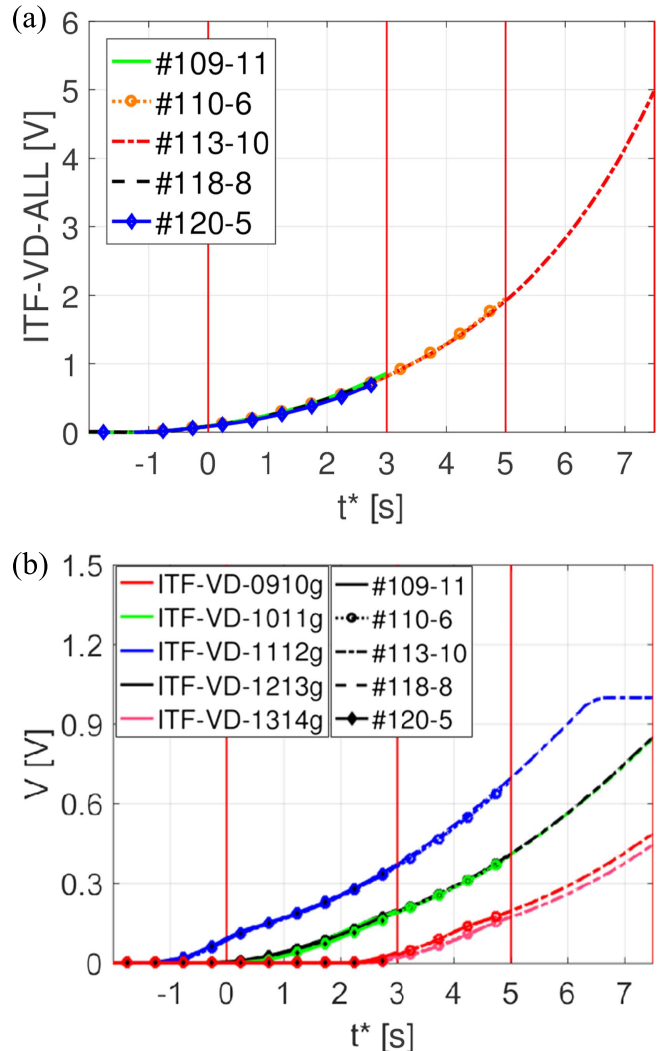


Figure 12. Measured evolution of the (a) total and (b) local voltages during TFI quench tests for shot #109–11 (solid), #110–6 (dotted with circles), #113–10 (dash-dotted), #118–8 (dashed) and #120–5 (solid with diamonds). In (b) different colors refer to different local sensors, while different line-styles refer to different experimental shots.

as a result of a not perfect attachment of the sensor to the jacket, resulting in an additional thermal contact resistance.

The reproducibility of the results in the TFI quench tests is confirmed also for the pressurization at the coil boundaries, which substantially shows the same behavior for all the shots, see figure 16(a), even during the quench initiation, as highlighted in

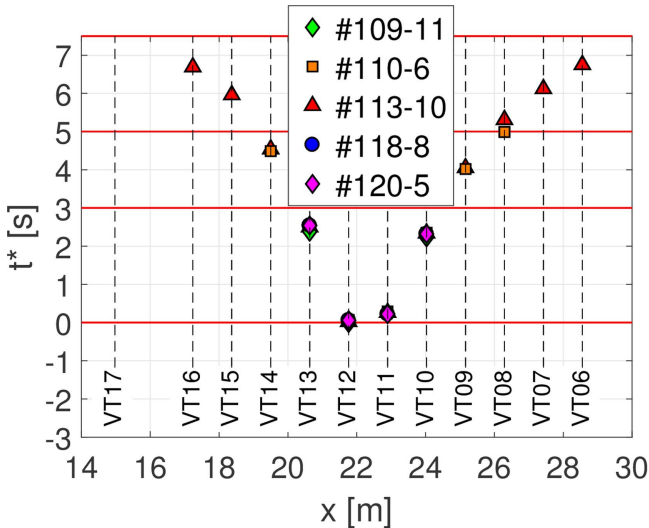


Figure 13. Measured propagation of the normal zone. The IH02 location is around 22.1 m.

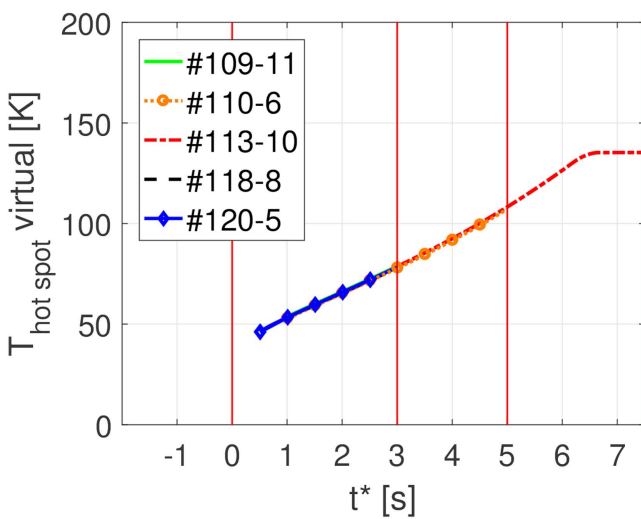


Figure 14. Evolution of the virtual hot spot temperature deduced from the VD_{1112} measurement (see text). The trace for shot #113–10 ($t_{\text{delay}} = 7.5$ s) flattens at ~ 140 K due to the saturation of the VD_{1112} voltage signal, see figure 12(b).

the zoom reported in figure 16(b). The maximum pressurization reaches almost 1.5 bar at the inlet, in the test with the maximum delay.

The mass flow rate shows an evolution independent of the particular quench scenario only after the QD or so, see figure 17; on the contrary, the evolution presents some differences in the quench initiation phase, especially between $t^* = -1.5$ s and -0.5 s, as shown in figure 17(b), which do not seem to be related, e.g., to the amount of the energy deposited (see also table 3).

About 1 s before the QD, the pressure at the boundaries increases very rapidly, see figure 16(b), because the Joule heating in the initiated normal zone at the center of the conductor causes a fast He expansion. This in turn causes, on the sound propagation time-scale between the normal zone and the TFI endings (~ 0.1 s), the He expulsion from the coil

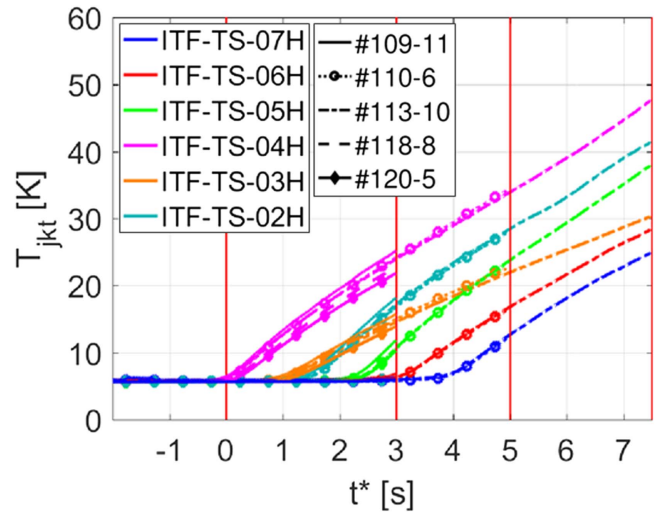


Figure 15. Measured evolution of the jacket temperature at different locations (see also figure 3) during the quench propagation. Different colors refer to different local sensors, while different line-styles refer to different experimental shots.

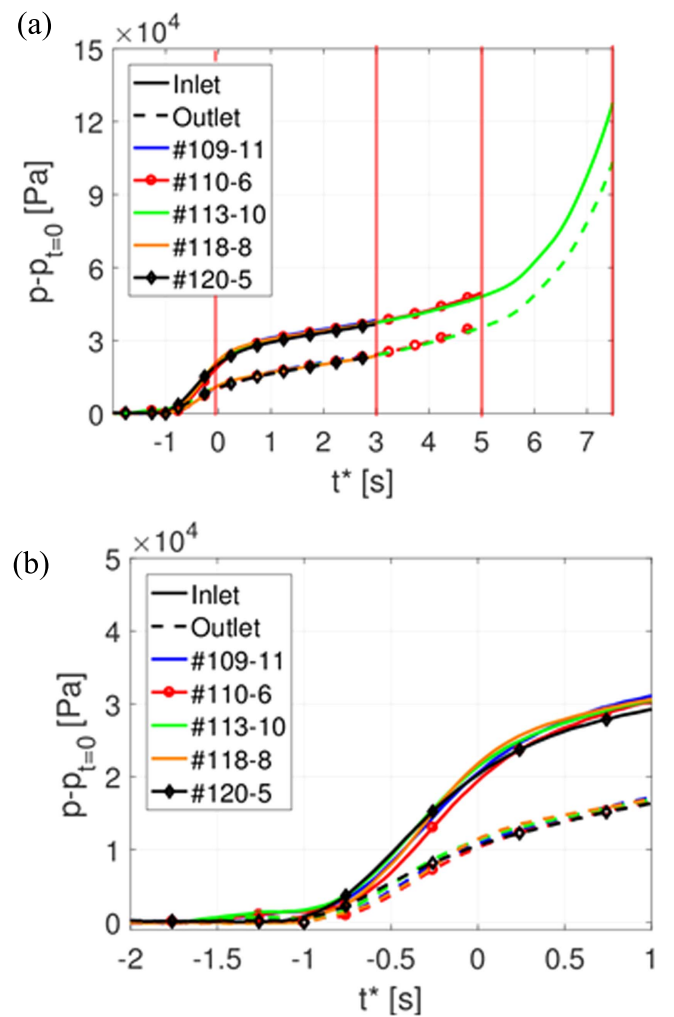


Figure 16. Measured evolution of the pressurization at the TFI boundaries (a) and zoom on the first phase of the transient (b) both at the inlet (solid) and outlet (dashed) of the coil for shot #109–11 (blue), #110–6 (red with circles), #113–10 (green), #118–8 (orange) and #120–5 (black with diamonds).

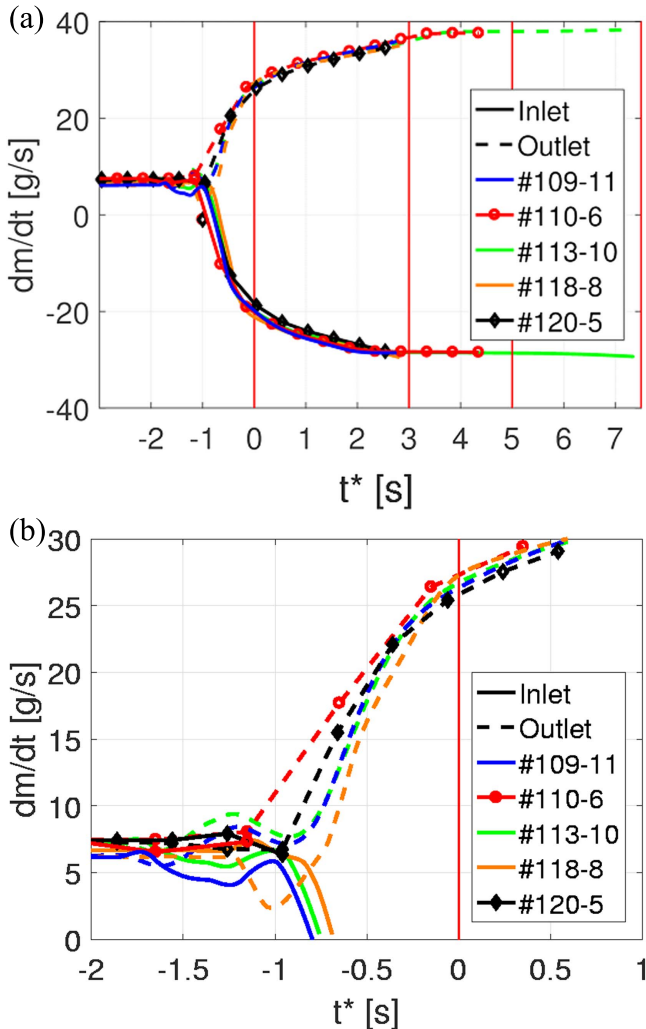


Figure 17. Measured mass flow rate evolution at the TFI boundaries (a) and zoom on the first phase of the transient (b) both at the inlet (solid) and outlet (dashed) of the coil for shot #109–11 (blue), #110–6 (red with circles), #113–10 (green), #118–8 (orange) and #120–5 (black with diamonds).

boundaries, see figure 17(b). Then, between $t^* = 0$ s and 1 s, the pressurization slows down consistently because of the reduction of the He expulsion, due in turn to the above-mentioned pressurization at the boundaries (the He expulsion being driven by the pressure difference between the quenched zone and the coil boundaries).

The second fast pressurization phase, for $t^* > 5$ s, already noticed in the CSIC tests [17], is possibly related to the quench acceleration reported in figure 13; the flow meters do not show a further He expulsion increase in this phase because their signal saturates for $t^* > \sim 3$ s, see figure 17(a). Since the flow meter is of the orifice type, the data outside the calibrated range, which goes from zero to around 30 g s^{-1} , are not reliable. For this reason, they will not be reported anymore from figure 17(b) onwards.

In the case of quench initiation using two IHs, shot #118–8, no major differences are present with respect to the shots where only one IH was used. The only effect of

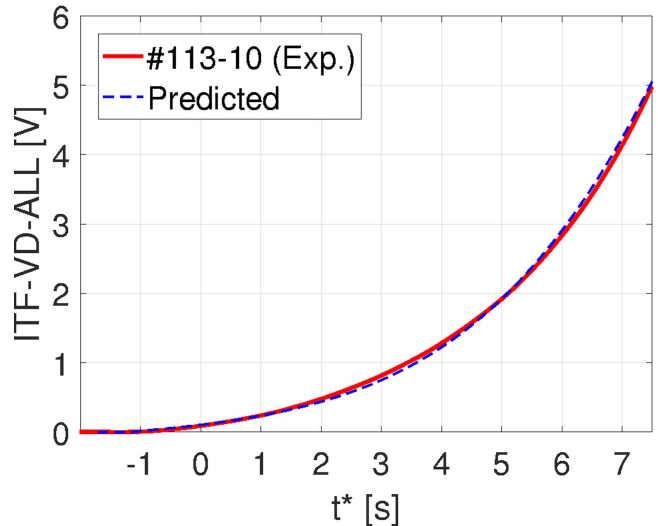


Figure 18. Comparison between predicted (thin dashed line) and measured (thick solid line) total voltage traces.

using two IHs is to deposit more energy than the required MQE, but that does not affect the quench propagation.

5. Comparison between 4C code predictions and measurements

For this comparison, only shot #113–10 will be considered, since it presents the longest delay time and, as such, it is the most interesting and severe from the quench propagation point of view. As the present work focusses on the quench *propagation* phase, between detection and dump, for the sake of the present comparison the results will be reported below as a function of a single time coordinate t^* , i.e. the real time shifted by the *respective* QD time. (For the sake of completeness we just quote here that $t_{\text{QD}}^{\text{pred}} \sim 1.71$ s, whereas $t_{\text{QD}}^{\text{exp}} \sim 1.64$ s. This obviously implies that the predicted and measured curves are not exactly synchronized in reality.) The details of the transient before the QD are indeed strongly dependent on uncertain parameters like the amount of energy actually deposited by the IH and its repartition between cable and jacket, which are beyond the scope of the present paper as they are known to have a negligible influence on the quench propagation phase. A separate study of the TFI IH-driven test results is ongoing, specifically devoted to the phase before the quench is initiated, and it will be presented elsewhere [33].

The predicted evolution of the total voltage across the TFI coil is almost indistinguishable from the measurement, see figure 18.

However, if we look in more detail at the evolution of the local voltages across pairs of neighboring voltage taps, see figure 19, we note that the perfect agreement in the global voltage is also partly the result of the casual compensation of small disagreements: indeed, the local predicted voltages take off a bit earlier than in the experiment, but then evolve a bit slower.

The comparison of the different hot spot predictions with the virtual thermometer, see figure 20, shows a good

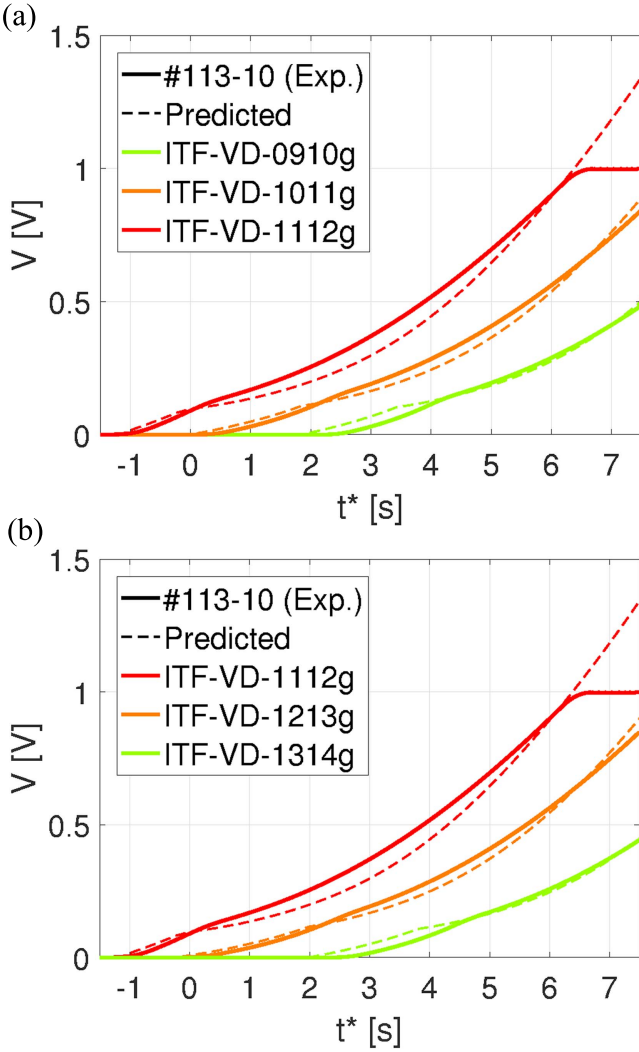


Figure 19. Comparison between predicted (thin dashed line) and measured (thick solid line) local voltage traces: (a) taps downstream of the IH02; (b) taps upstream of the IH02.

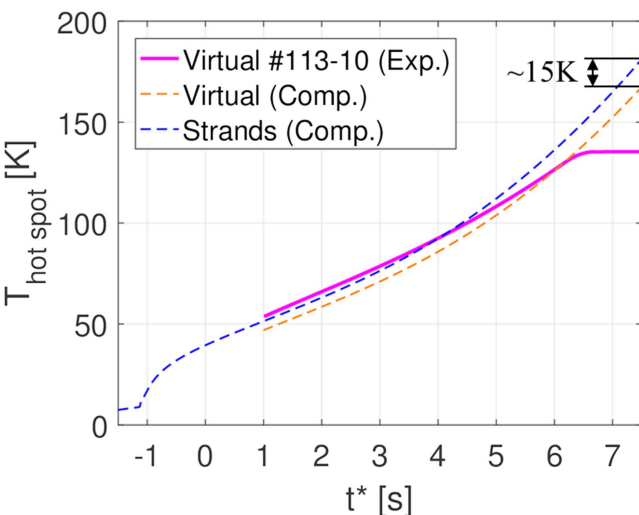


Figure 20. Hot spot virtual temperature for experimental (thick solid red) measurement, predicted virtual (thin orange dashed) and strand (thin dashed blue) hot spot temperature.

agreement between prediction and measurement, although the prediction somewhat overestimates the rate of hot spot temperature increase ($\sim 24 \text{ K s}^{-1}$ against $\sim 19 \text{ K s}^{-1}$ measured at $t^* = 6 \text{ s}$). As the predicted max strands temperature is less than 15 K above the hot spot temperature predicted by the virtual thermometer, we can now reasonably estimate the actual maximum strand temperature adding 15 K to the extrapolated virtual thermometer measurement ($\sim 155 \text{ K}$) just before the current dump, resulting in our best hot spot temperature estimate of $\sim 170 \text{ K}$. The fact that the 7.5 s delay quench in the TFI was conducted to mimic the real ITER TF behavior allows considering this hot spot temperature as reasonably representative of the expected actual value after a quench in a TF coil: being it still well below 250 K, it satisfies the ITER design criteria [34].

The comparison between predicted and measured quench propagation speed shows a good agreement, with an error always below 15%, in the initial and central phase of the quench propagation, up to $t^* \sim 5 \text{ s}$, as shown in figure 21. On the contrary, in the last phase the predicted quench propagation speed is much smaller than measured, i.e. the quench is accelerating much more than predicted, with errors up to almost 50%. It should be noted that in previous quench studies, e.g. [12, 15, 17], an agreement like that shown in figure 21(a) was typically considered to be globally very good, but the punctual representation of the error in the quench propagation speed given in figure 21(b) conveys a somewhat different picture.

The respective symbols in figure 21 are located in space at the generic tap location and in time when the local voltage across two neighboring taps reaches 1 mV, see figure 22 for an example. It is seen from this figure that the 1 mV threshold is suitably chosen to stay just above the noise level in the measurement.

Despite the very good agreement between prediction and measurements shown above, the predicted jacket temperatures significantly overestimate the experimental results, see figure 23, and tend to rise earlier and faster. This level of disagreement was unexpected, since in previous quench simulations, e.g., in the case of the CSIC, the 4C code had shown a very good capability to reproduce the jacket temperature evolution [17], even if the jacket was thick and square instead of thin and circular.

One possible explanation for the discrepancy between predicted and measured jacket temperatures is that the Cernox thermometers are in reality glued on the external surface of the jacket, see figure 24, and the glue layer, not included in our model, delays the response of the sensor to the evolution of the jacket temperature. As a last comment on this point, similar results to those predicted with 4C (and therefore similar disagreement with the experiment) were also found after the tests in analyses performed with another computational tool, the Supermagnet code [35], by other authors [36].

The predicted mass flow rate evolution, see figure 25, shows two distinct phases. In the first one, just after the IH pulse, we have a complete disagreement between prediction and measurement: while, e.g., the predicted He flow reverses at the TFI inlet, as intuitively expected, the measured one

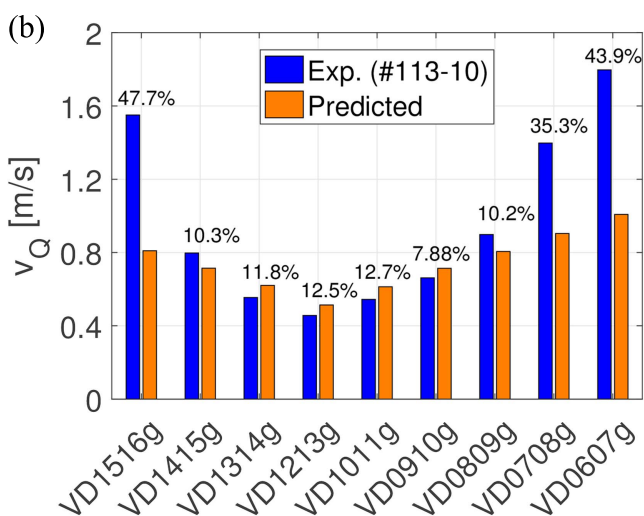
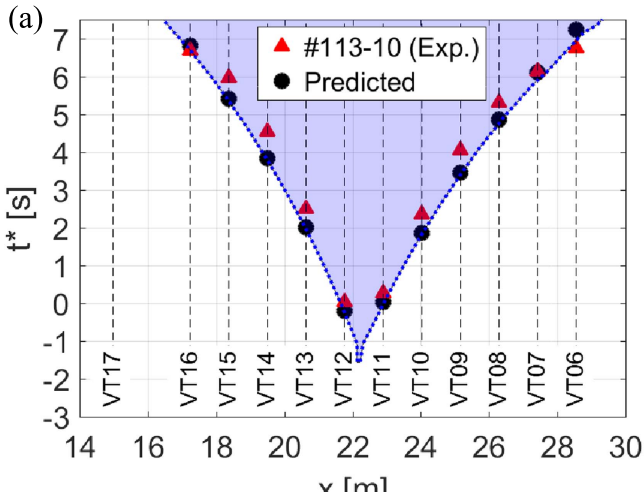


Figure 21. (a) Comparison of predicted (black circles) versus measured (red triangles) quench front propagation; the trajectory of the computed points where $I = I_c$ is also reported (dotted blue line). (b) Comparison of predicted (orange) versus measured (blue) quench propagation speed at different locations of the quench front. The relative error in the prediction is indicated in %.

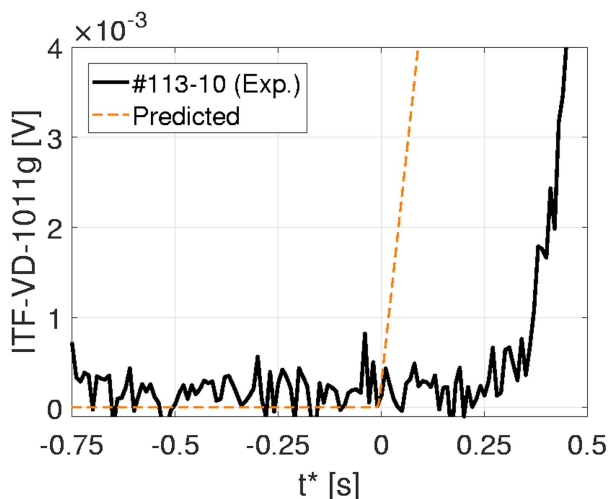


Figure 22. Predicted and measured evolution of the ITF-VD-1011g voltage (right downstream the IH02) in the quench initiation phase.

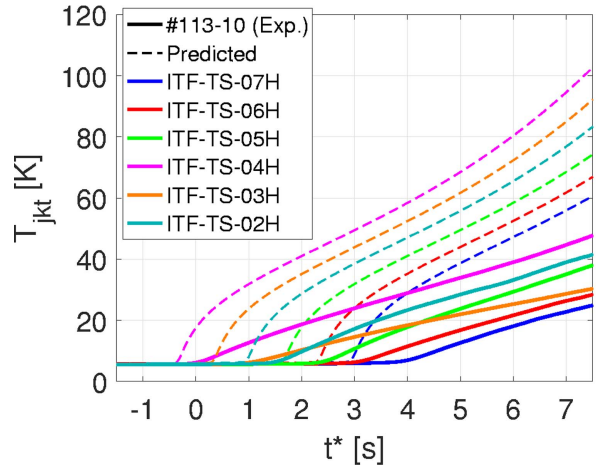


Figure 23. Comparison between measured (thick solid) and predicted (thin dashed) jacket temperature evolutions.

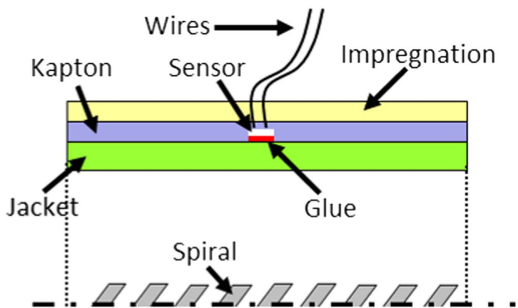


Figure 24. Sketch showing how the Cernox temperature sensor is attached to the jacket.

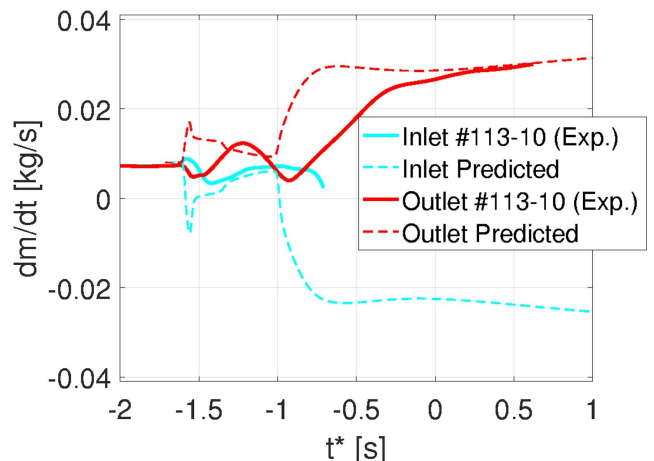


Figure 25. Comparison between measured (solid thick) and predicted (thin dashed) mass flow rate evolution at inlet (cyan) and outlet (red) of the coil.

increases, albeit only slightly (the opposite happens at the outlet, where instead of the predicted, and intuitive, initial increase of the flow, a reduction of the flow is recorded by the flow meter). This feature, already noted in the last CSIC test, remains therefore unexplained. In the second phase, an anticipated and stronger expulsion of the helium at the outlet is predicted by the model, compared with the measurement. This difference is due to the fact that in the experiment the He

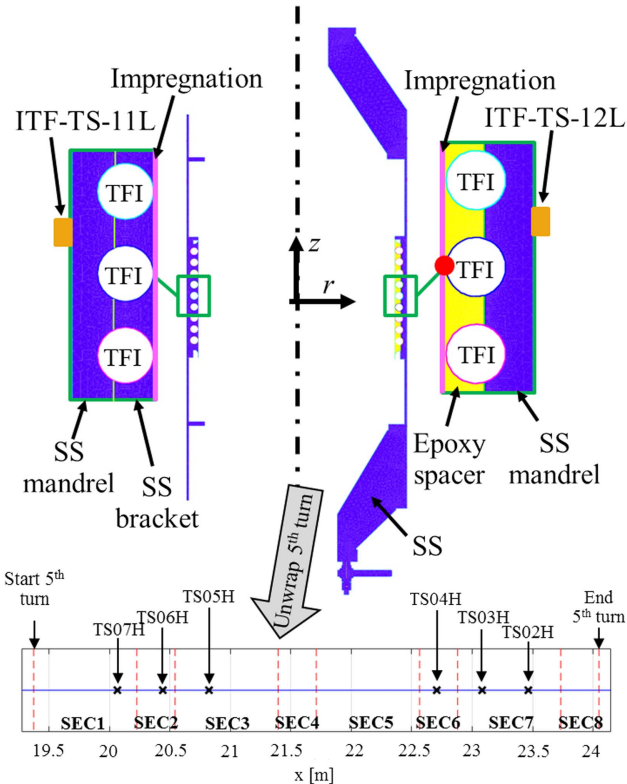


Figure 26. Top: sketch of the structures model implemented in 4C code showing the geometry of the conductor grooves and the additional temperature monitor used in the simulations, on the 5th turn, at the boundary between the structures and the CICC, indicated by the red solid circle. The location of the mandrel temperature sensors is also reported (orange rectangles). Bottom: location of the jacket temperature sensors on the central turn with respect to the position of the cuts used to discretize the 3D structures.

expulsion from the coil tends to pressurize the manifolds at the coil boundaries, in turn reducing the pressure difference between the quenched zone and the coil boundaries that drives the He expulsion, see above.

6. Interpretive 4C code simulations of the TFI quench

The focus of the interpretive simulations, performed *after* the test and presented in this section, is on trying to improve the model especially considering the quantities not well reproduced by the predictive simulations. These include the jacket temperature and the quench acceleration in the last phase of the propagation before the dump as well as the inlet/outlet mass flow rates (and pressurizations).

6.1. Including the structures in the model

The first addition to the predictive model is the model of the structures. The rationale for this addition is that we want to check if the measured jacket temperature is at least bracketed by the computed jacket and structure temperatures.

The SS mandrel, holding the TFI, was discretized azimuthally in 8 2D ‘cuts’ where the heat conduction problem is solved with the finite element method, see figure 26. The

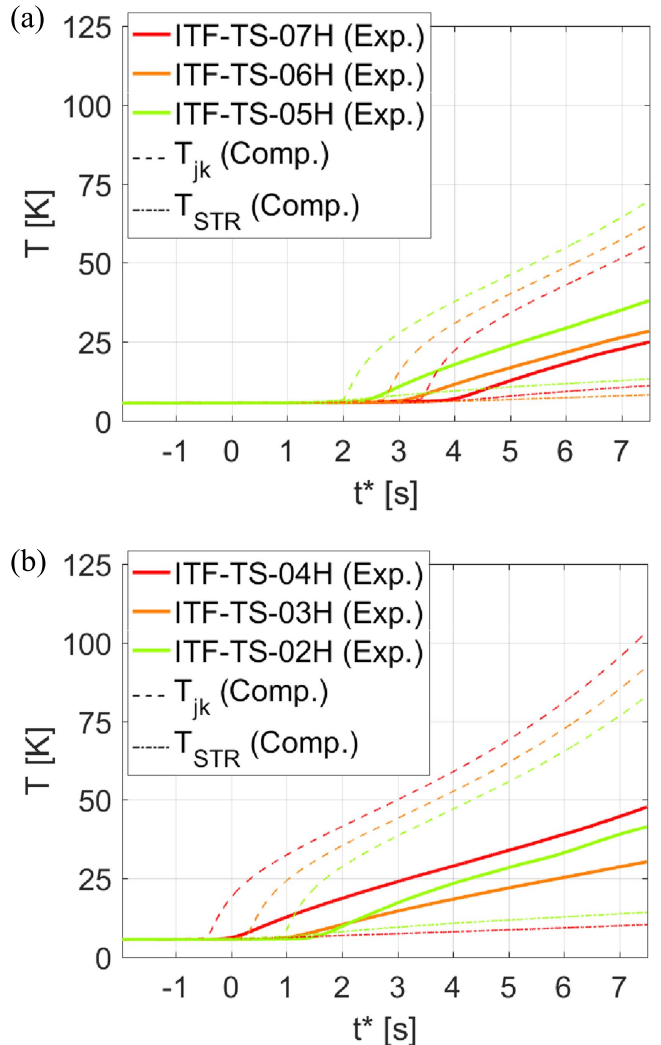


Figure 27. Measured jacket temperature evolution for shot #113–10 (thick solid lines) versus computed jacket temperatures (thin dashed lines) and computed structure temperatures at the additional monitor location (thin dash-dotted lines), see figure 26, for temperature sensors (a) upstream and (b) downstream the quench initiation zone.

number of sections, as well as the number of triangles into which each section has been discretized (from 6500 to 22 000 triangles, depending on the particular cut considered), have been defined based on our previous experience on similar geometries [37] and transients [38].

The structures temperature is monitored at selected locations on the 2D cuts, as indicated in figure 26.

As expected, it turns out that the computed jacket and structure temperatures bracket the measured jacket temperatures, see figure 27.

The addition of the structures in the interpretive model also allows computing the mandrel temperature at the sensors ITF-TS-11L and ITF-TS-12L, located on the external surface of the SS mandrel in correspondence of the 5th TFI turn as shown in figure 26. The computed results are in qualitative agreement with the measured temperature evolutions, see figure 28. The quantitative discrepancy may be related to the

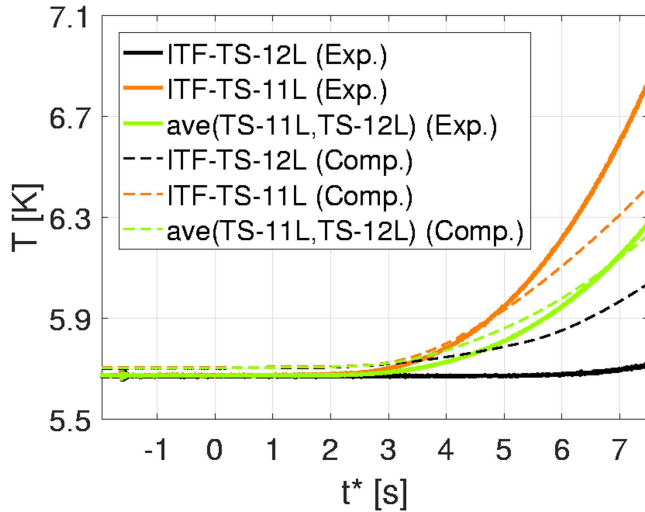


Figure 28. Comparison between measured (thick solid) and computed (thin dashed) mandrel temperature evolution at ITF-TS-12L (black) and ITF-TS-11L (orange) sensor location. The computed and measured average temperatures are also reported.

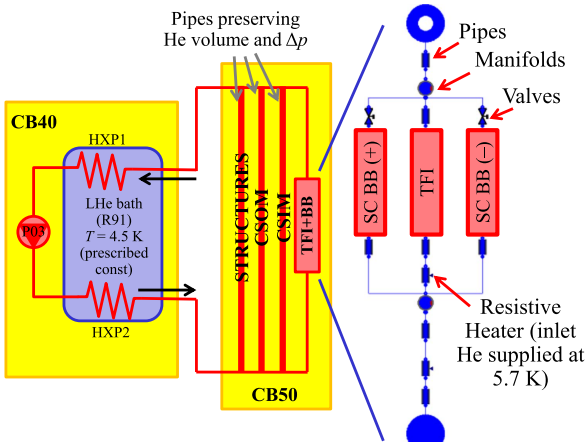


Figure 29. Cryogenic circuit model (HX = heat exchanger, LHe = liquid Helium, CB = cold box, P# = cold circulator).

fact that the FE model adopted features a finite number of 2D sections; as a result, the virtual sensors, located at the same (r , z) position of the real sensors, are actually representative of a toroidal segment of the mandrel, while the temperature measurement obviously refers to a single toroidal coordinate. Indeed, the agreement in the evolution of the *average* mandrel temperature between the two locations is very good.

6.2. Including a different treatment of the boundary conditions

The second modification/extension of the predictive model, implemented for the interpretation after the tests, is to use either of the following two improved alternative recipes for the boundary conditions:

- include an external cryogenic circuit to avoid the need of boundary conditions [39] (since in principle this recipe cannot be better than the second recipe in an interpretive simulation, it is only justified by the interest

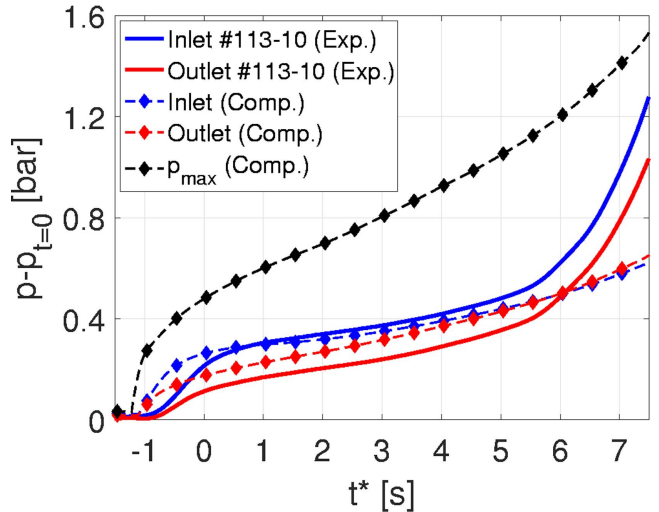


Figure 30. Comparison between measured (thick solid) and simulated (thin dashed with diamonds) inlet (blue) and outlet (red) pressure. The maximum pressure in the conductor is also reported (thin dashed black with diamonds). All pressures are rescaled to the respective initial values.

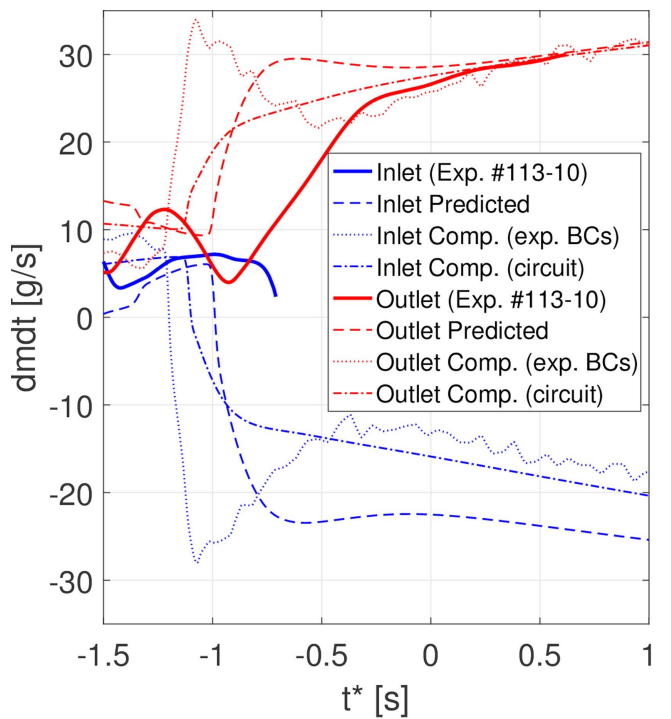


Figure 31. Evolution of measured (thick solid), predicted (thin dashed), computed with experimental BCs (thin dotted) and computed with circuit (thin dash-dotted) mass flow rates at inlet (blue) and outlet (red) of the TFI coil.

to model also $p_{in}(t)$, $p_{out}(t)$, $T_{in}(t)$ and compare them with the measurements);

- adopt the *measured* $p_{in}(t)$, $p_{out}(t)$, $T_{in}(t)$.

According to recipe (i), a simplified model of the TFI, bus bars (BBs) and CSMC inner module (CSIM) and outer module (CSOM) cooling circuits, the latter included in the model as simple pipes, just to preserve the main features of

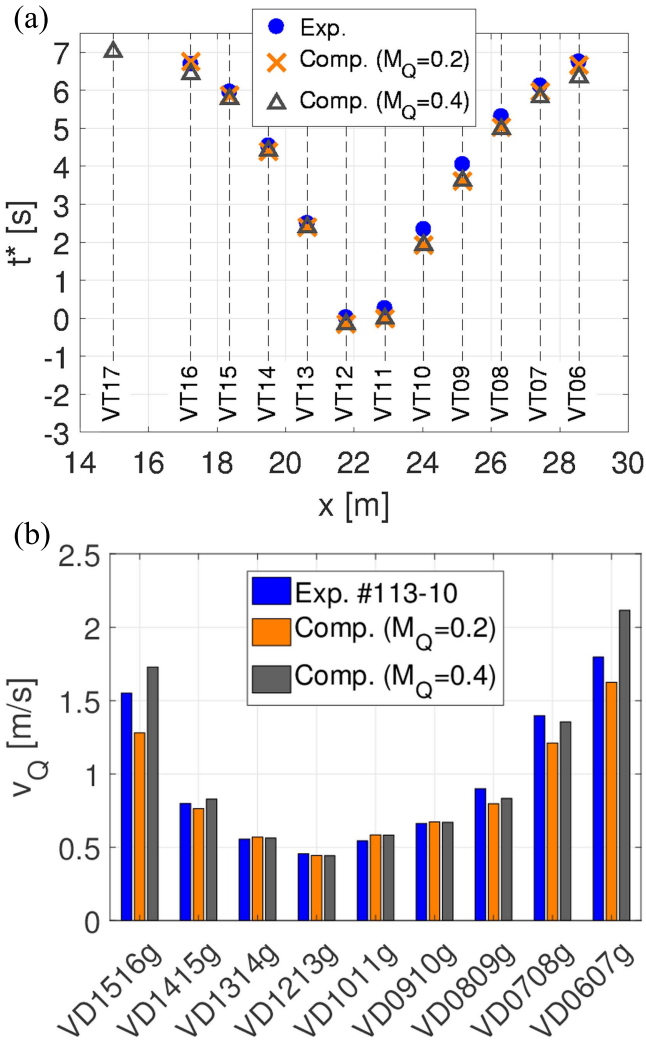


Figure 32. (a) Normal zone propagation with two different multipliers M_Q of the inter-turn thermal coupling. (b) Comparison of measured (blue) and computed with two values of M_Q (grey and orange, respectively) quench propagation speed at different locations of the quench front.

the real circuit, has also been implemented, following a similar model adopted in [17] for the CSIC, see figure 29, as an alternative to imposing the measured boundary conditions.

The agreement of the simulated pressurization at the TFI boundaries with the measurement, see figure 30, is only qualitative even for $t^* < 5$ s: the pressurization is anticipated by the code, consistently with the anticipated He expulsion shown in figure 31.

The second phase of the quench propagation (for $t^* > 5$ s), characterized as observed above by an accelerated pressurization at the TFI boundaries, is not properly captured by the simulation even in this case.

Adopting recipe (ii) above, the measured He mass flow rates at the inlet and outlet of the coil are not better reproduced, compared to the 4C predictions with fixed BCs, see figure 25 above.

As expected [39], the computed propagation is also slower than what was found above in the predictive runs, due to the pressurization at the boundaries.

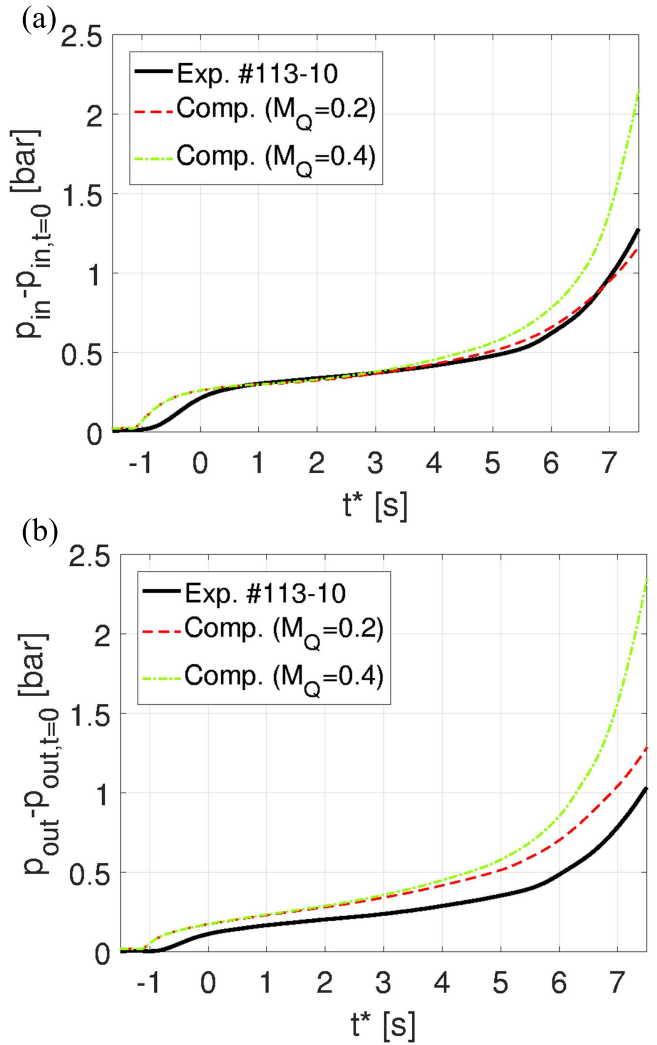


Figure 33. Comparison between measured (thick solid black) and simulated with two values of M_Q (thin dashed red and thin dash-dotted green, respectively) inlet (a) and outlet (b) pressure. All pressures are rescaled to the respective initial values.

6.3. Parametric study of the effects of inter-turn heat transfer

In order to try and address the question of the lasting discrepancy between simulated and measured acceleration of quench and pressurization at the boundaries for $t^* > 5$ s, it may be useful to observe that it takes about that time for the quench to propagate both upstream and downstream along an entire turn, i.e., to reach again the azimuthal region where the IH is located.

Since it is well known, see e.g. Figure 8, that preheating ahead of the quench front is the cause of quench acceleration, we conjecture that the actual inter-turn heat transfer is much more effective than what hypothesized so far. In particular, a third set of interpretive simulations was carried out, where the central turn (on which the IH is installed) is thermally coupled to the two neighboring ones directly across the $\delta_{ins} = 1.4$ mm thick turn insulation, i.e. neglecting the presence of the structures in between. The contact perimeter is assumed equal to its maximum value, i.e. half of the jacket circumference. (Clearly, although this increased coupling is assumed to act

Table 4. Qualitative evaluation of the agreement between ITER-relevant Nb₃Sn quench simulations and experiments.

Reference	Prediction	$V_{\text{tot}}(t^*)$	$V_{\text{loc}}(t^*)$	$T_{\text{hot spot}}(t^*)$	$V_q(t^* < 5 \text{ s})$	$V_q(t^* > 5 \text{ s})$	$T_{jk}(t^*)$	$dm/dt(t^*)$	$p(t^*)$
Present work	😊	😊	😊😊	😊😊	😊😊	😊😊	😊?	😊?	😊😊
[17]	NA	😊😊	😊😊	😊😊	😊😊	😊😊	😊	😊?	😊?
[15]	NA	😊😊	NA	😊	😊	😊😊	NA	NA	NA
[14]	NA	😊😊	NA	😊😊	😊	😊😊	NA	NA	NA
[13]	NA	😊	NA	NA	NA	NA	NA	NA	NA
[12]	NA	😊😊	NA	😊	😊	😊😊	😊	😊	😊
[5]	NA	😊😊	NA	NA	😊😊	😊😊	NA	NA	😊😊

Note: multiple faces = agreement evaluated between the two, or either of the two depending on the particular sub-feature (e.g., V_q upstream or downstream); ? = possible uncertainties in the accuracy of experimental data.

all along the three turns, it will be most effective where the temperature differences are significant, i.e., below the IH). As this should give the maximum possible thermal coupling among the turns, the inter-turn heat transfer coefficient HTC_{IT} computed across the nominal insulation thickness $2 \times \delta_{\text{ins}}$ is then parametrically scaled by a factor M_Q between 0 and 1 as follows:

$$\text{HTC}_{\text{IT}} = M_Q \times k_{\text{ins}} / (2 \times d_{\text{ins}}), \quad (8)$$

where k_{ins} is the thermal conductivity of the insulation material.

The results of the present sensitivity study are presented in figure 32, where it is seen that, with two suitable values of M_Q , it is possible to at least bracket the measured evolution of the quench propagation.

Also the accelerated pressurization for $t^* > 5 \text{ s}$ at both inlet and outlet is now better captured, at least qualitatively, see figure 33.

7. Conclusions

The results of the predictive analysis, of the experimental tests performed at QST Naka, Japan, and of the interpretive analysis of quench propagation in the ITER Nb₃Sn toroidal field insert coil have been presented and compared.

The quenches were initiated using an IH, as customary for the ITER insert coils, and the results of tests adopting different delay times between QD and TFI current dump generally showed excellent reproducibility.

All the simulations presented in the paper have been performed with the 4C code and a qualitative summary of the level of success of the code in reproducing the evolution of the single, detailed features of quench propagation is reported in table 4, together with a similarly qualitative evaluation of the results of previous assessments of quench propagation in other ITER-relevant Nb₃Sn coils available in the literature.

Most of the experimental results show excellent reproducibility in the quench tests performed with different delays: in the longest, 7.5 s delay test, the global voltage across the coil increased up to $\sim 5 \text{ V}$, the hot spot temperature increased up to $\sim 170 \text{ K}$, and the quench accelerated from ~ 0.5 to $\sim 1.5 \text{ m s}^{-1}$, both upstream and downstream.

Predictions performed using the 4C code, and rigorously issued before the tests, to the best of our knowledge for the

first time for an ITER-relevant quench, turned out to be in good-to-excellent agreement with the measurements for most of the relevant quantities (global and local voltages, hot spot temperature, quench propagation speed). However, the further acceleration of the quench and of the related pressurization at the coil inlet and outlet, occurring in the last third ($\sim 2.5 \text{ s}$) of the longest test, were not captured by the predictive simulation. It should be noted, however, that especially concerning the quench propagation speed a much more severe and detailed diagnostics was introduced here, see figure 21(b), whereas in the past, see the references considered in table 4, an agreement like that shown in figure 21(a) would have been likely commented as globally excellent.

A major discrepancy was found in the jacket temperatures, whose dynamics was predicted to be much faster than measured. This is particularly surprising, considering that excellent agreement had been recently reported between 4C simulations and measurements, notwithstanding the much thicker jacket, in the otherwise relatively similar case of the ITER CSIC coil [17]; we speculate that this disagreement might be at least partly due to an issue of attachment of the sensors to the jacket and related contact thermal resistance. Also the dynamics of the He expulsion at the coil inlet and outlet was well predicted by 4C, except for the very initial phase before QD, which is likely to be very dependent on the details of the IH power deposition in the conductor and of the operating conditions at the time of the IH pulse. The very first phase of the measured mass flow rate evolution after the IH pulse contains an odd feature (dm/dt increasing at the inlet and decreasing at the outlet), already noticed in the CSIC quench test but not captured by the simulations and still unexplained.

The last part of the paper was devoted to the interpretive analysis of the longest delay quench, where we attempted to improve the model by including the structures (mandrel, etc) and by either substituting the fixed values imposed as boundary conditions in the predictions with measured time dependent values, or adding a model for the external cryogenic circuit to avoid the need of boundary conditions in the first place. While these extensions allowed to include in the comparison between simulations and measurements also inlet/outlet pressures and mandrel temperatures, showing qualitative agreement, they did not lead to noticeable improvement in the features where a significant disagreement had been found as discussed above.

To better capture the further acceleration of the quench and of the related pressurization at the coil inlet and outlet, occurring in the last third (~ 2.5 s) of the longest test, the effect of an enhanced inter-turn thermal coupling, with respect to that assumed in the predictive simulations and then modeled through the structures module in the interpretive simulations, was parametrically studied. This allowed the bracketing of the acceleration of both the quench and the pressurization measured in the last phase of the longest quench test (7.5 s delay).

Acknowledgments

The PhD fellowship of AB is partially financially supported by EUROfusion. AB, LS and RZ thank QST Naka for the kind hospitality during the TFI tests. This work was done in the framework of the ‘Arrangement for Manufacturing and Testing of the CS Insert Coil and TF Insert Coil Related to the ITER Magnet Systems’ between JAEA (now QST) and ITER IO, endorsed by the USIPO. The participation of the Politecnico di Torino to the TFI test and analysis was under an Assignment Agreement between Politecnico di Torino and QST.

We also wish to thank the three anonymous referees for their very constructive comments and hints, which led in our opinion to a significant improvement of the paper.

ORCID iDs

R Zanino  <https://orcid.org/0000-0003-0334-8275>

References

- [1] Oberkamp W L and Roy C J 2012 *Verification and Validation in Scientific Computing* (Cambridge: Cambridge University Press)
- [2] Roache P J 1998 *Verification and Validation in Computational Science and Engineering* (Albuquerque, NM: Hermosa)
- [3] Dresner L 1989 Quench pressure, thermal expulsion, and normal zone propagation in internally cooled superconductors *IEEE Trans. Magn.* **25** 1710–2
- [4] Anghel A 1998 QUELL experiment: analysis and interpretation of the quench propagation results *Cryogenics* **38** 459–66
- [5] Zanino R, Bottura L and Marinucci C 1997 A comparison between 1- and 2-fluid simulations of the QUELL conductor *IEEE Trans. Appl. Supercond.* **7** 493–6
- [6] Zanino R, Bottura L and Marinucci C 1998 Computer simulation of quench propagation in QUELL *Adv. Cryog. Eng.* **43** 181–8
- [7] Martovetsky N et al 2002 Test of the ITER central solenoid model coil and CS insert *IEEE Trans. Appl. Supercond.* **12** 600–5
- [8] Martovetsky N et al 2003 Test of the ITER TF insert and central solenoid model coil *IEEE Trans. Appl. Supercond.* **13** 1441–6
- [9] Okuno K et al 2003 Test of the NbAl insert and ITER central solenoid model coil *IEEE Trans. Appl. Supercond.* **13** 1437–40
- [10] Bessette D et al 2009 Test results from the PF conductor insert coil and implications for the ITER PF system *IEEE Trans. Appl. Supercond.* **19** 1525–31
- [11] Martovetsky N et al 2016 ITER central solenoid insert test results *IEEE Trans. Appl. Supercond.* **26** 4200605
- [12] Savoldi Richard L, Salpietro E and Zanino R 2002 Inductively driven transients in the CS insert coil (II): quench tests and analysis *Adv. Cryog. Eng.* **47** 423–30
- [13] Takahashi Y, Yoshida K, Nabara Y, Edaya M and Mitchell N 2006 Simulation of quench tests of the central solenoid insert coil in the ITER central solenoid model coil *IEEE Trans. Appl. Supercond.* **16** 783–6
- [14] Inaguchi T, Hasegawa M, Koizumi N, Isono T, Hamada K, Sugimoto M and Takahashi Y 2004 Quench analysis of an ITER 13 T-40 kA Nb₃Sn coil (CS insert) *Cryogenics* **44** 121–30
- [15] Savoldi Richard L, Portone A and Zanino R 2003 Tests and analysis of quench propagation in the ITER toroidal field conductor insert *IEEE Trans. Appl. Supercond.* **13** 1412–5
- [16] Zanino R, Bonifetto R and Savoldi Richard L 2010 Analysis of quench propagation in the ITER poloidal field conductor insert (PFCI) *IEEE Trans. Appl. Supercond.* **20** 491–4
- [17] Bonifetto R, Isono T, Martovetsky N, Savoldi L and Zanino R 2017 Analysis of quench propagation in the ITER central solenoid insert (CSI) coil *IEEE Trans. Appl. Supercond.* **27** 4700308
- [18] Zanino R and Savoldi Richard L 2013 Multiscale approach and role of validation in the thermal-hydraulic modeling of the ITER superconducting magnets *IEEE Trans. Appl. Supercond.* **23** 4900607
- [19] Ozeki H et al 2016 Manufacture and quality control of insert coil with real ITER TF conductor *IEEE Trans. Appl. Supercond.* **26** 4202504
- [20] Savoldi Richard L, Casella F, Fiori B and Zanino R 2010 The 4C code for the cryogenic circuit conductor and coil modeling in ITER *Cryogenics* **50** 167–76
- [21] Tsuji H et al 2012 Progress of the ITER central solenoid model coil program *Nucl. Fusion* **52** 645–51
- [22] Takahashi Y et al 2012 Mass production of Nb₃Sn conductors for ITER toroidal field coils in Japan *IEEE Trans. Appl. Supercond.* **22** 4801904
- [23] Naka Fusion Institute Superconducting Coil Test Group 2016 Database of TF Insert Coil Experiment in 2016 *National Institutes for Quantum and Radiological Science and Technology* (former JAEA) report (unpublished).
- [24] Bottura L and Bordini B 2009 $J_c(B, T, \varepsilon)$ parameterization for the ITER Nb₃Sn production *IEEE Trans. Appl. Supercond.* **19** 1521–4
- [25] ITER design description document (DDD) 11-2 magnets, TF coils and structures 2009 *ITER_D_2MVZNX v2.2*
- [26] Savoldi L and Zanino R 2000 Thermal-hydraulic analysis of T_{CS} measurement in conductor 1 A of the ITER central solenoid model coil using the M&M code *Cryogenics* **40** 593–604
- [27] Zanino R, Bonifetto R, Heller R and Savoldi Richard L 2011 Validation of the 4C thermal-hydraulic code against 25 kA safety discharge in the ITER toroidal field model coil (TFMC) *IEEE Trans. Appl. Supercond.* **21** 1948–52
- [28] Zanino R, Bonifetto R, Hoa C and Savoldi Richard L 2014 Verification of the predictive capabilities of the 4C code cryogenic circuit model *AIP Conf. Proc.* **1573** 1586–93
- [29] Khodak A E, Martovetsky N, Smirnov A V and Titus P H 2014 Analysis of TF insert coil *IEEE Trans. Appl. Supercond.* **24** 4201304
- [30] Bonifetto R, Isono T, Martovetsky N, Savoldi L and Zanino R 2017 Analysis of the DC performance of the ITER CSI coil using the 4C code *Fusion Eng. Des.* **124** 159–62

- [31] Brighenti A, Bonifetto R, Isono T, Martovetsky N, Ozeki H, Savoldi L and Zanino R 2017 Thermal-hydraulic characterization of the ITER toroidal field insert coil *Presented at the European Conf. on Applied Superconductivity* <https://indico.cern.ch/event/659554/contributions/2716452/>
- [32] Lue J W, Dresner L, Schwenterly S W, Wilson C T and Lubell M S 1993 Investigating thermal-hydraulic quenchback in a cable-in-conduit superconductor *IEEE Trans. Appl. Supercond.* **3** 338–41
- [33] Savoldi L et al 2017 private communication
- [34] ITER design description document (DDD) 11-7 magnets, conductors 2009 *ITER_D_2NBKXY v1.2*
- [35] Bagnasco M, Bessette D, Bottura L, Marinucci C and Rosso C 2010 Progress in the integrated simulation of thermal-hydraulic operation of the ITER magnet system *IEEE Trans. Appl. Supercond.* **20** 411–4
- [36] Bessette D and Gauthier F 2017 private communication
- [37] Bonifetto R, Brighenti A, Isono T, Martovetsky N, Kawano K, Savoldi L and Zanino R 2017 Analysis of the cooldown of the ITER central solenoid model coil and insert coil *Supercond. Sci. Technol.* **30** 015015
- [38] Savoldi L, Bonifetto R, Brighenti A, Corato V, Muzzi L, Turtù S, Zanino R and Zappatore A 2017 Quench propagation in a TF coil of the EU DEMO *Fusion Sci. Technol.* **72** 439–48
- [39] Savoldi L, Bottura L and Zanino R 2000 Simulation of thermal-hydraulic transients in two-channel CICC with self-consistent boundary conditions *Adv. Cryog. Eng.* **45** 697–704